Engineering Geology 348 (2025) 107961

Contents lists available at ScienceDirect

Engineering Geology

journal homepage: www.elsevier.com/locate/enggeo

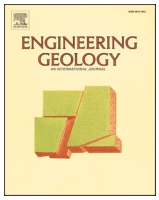

The long-term strength and creep behavior of fully saturated shaly Opalinus Clay

Lina Gotzen [a,*], Lisa Winhausen [a], Mohammadreza Jalali [a], Kavan Khaledi [b], Florian Amann [a,b]

[a] Department of Engineering Geology and Hydrogeology, RWTH Aachen, Aachen, Germany
[b] Fraunhofer Research Institution for Energy Infrastructures and Geotechnologies, Germany

ARTICLE INFO

Keywords:
Clay shale
Drained creep behavior
Multi-stage loading path
Effective long-term strength
Creep mechanisms

ABSTRACT

Long-term deformation in tunneling is typically associated with consolidation and creep, two time-dependent processes that may occur simultaneously and are superimposed. However, from tunnel convergence measurements these two processes cannot be distinguished. Thus, an accurate laboratory characterization of creep mechanisms under long-term in-situ conditions (i.e., fully saturated and drained) is required to improve numerical predictions for deep geological nuclear waste repositories. The laboratory study investigates the pure rheological creep behavior of shaly Opalinus Clay. After full re-saturation and consolidation of the specimens, a fully drained multi-stage creep test was performed. Time-dependent axial and radial deformations were monitored during creep stages of constant effective stress. The results show that the creep strain rates increase exponentially with increasing differential stress accompanied by a change in the dominant creep mechanism. Creep strain rates at low differential stresses up to 10 MPa are in the magnitudes of 10^{-11} s^{-1} and 10^{-10} s^{-1}, whereas creep rates in the magnitudes of 10^{-10} s^{-1} and 10^{-9} s^{-1} are observed at elevated differential stresses of more than 10 MPa, before initiation of tertiary creep, i.e., creep failure. Two thresholds for possible creep failure are presented, defining a stress-related long-term strength and a strain-related onset of tertiary creep.

1. Introduction

Opalinus Clay (OPA) is a clay shale formation that has been selected as the host rock for the future nuclear waste repository in Switzerland, and is considered a potential host rock in Germany. The disposal of high-level nuclear waste requires the construction of deep tunnels designed to meet performance requirements that exceed the service life of typical civil engineering constructions. To ensure the long-term safety and integrity, assessments must account for transient and coupled thermo-hydro-mechanical-chemical (THMC) processes throughout an entire lifecycle that may span up to one million years (Bossart et al., 2017). For low permeability clay shales (around 10^{-21} m^2), such as Opalinus Clay, quantitative predictions must address both the short-term deformation during construction as well as long-term deformation throughout open drift phases, waste emplacement, and the post-closure phase. In-situ observations of underground openings in these low permeability clay shales show ongoing convergence long after the construction phase (Barla, 2001; Armand et al., 2013). This convergence results from time-dependent deformation processes which can ultimately lead to delayed failure and changes in permeability or sealing integrity, even under stress conditions below the short-term strength of the rock (Bieniawski, 1967; Dusseault and Fordham, 1993). It is therefore crucial to gain a proper understanding of long-term deformation processes and their impact on the structural integrity of underground constructions with a prolonged lifetime, such as nuclear waste repositories (Aristorenas, 1992; Mánica et al., 2017).

Long-term deformation is typically associated with consolidation and creep, two intrinsically different phenomena that may occur simultaneously and may be superimposed (Taylor and Merchant, 1940; Terzaghi, 1943; Bui et al., 2001). Whereas consolidation is a coupled hydro-mechanical response driven by changes in the effective stress, creep is a purely rheological property of the ground that continues even after complete pore pressure dissipation. Leone et al. (2024) and Nordas et al. (2024) used coupled numerical modeling to study the impact of consolidation and creep on tunneling through squeezing ground. They found no qualitative differences in the transient evolution of convergences resulting from consolidation compared to those caused by creep. Thus, from typical tunnel monitoring data (i.e., convergence measurements) it is not possible to distinguish these time-dependent phenomena. This is even more challenging in low permeability rock, such as

* Corresponding author.
E-mail address: gotzen@lih.rwth-aachen.de (L. Gotzen).

https://doi.org/10.1016/j.enggeo.2025.107961
Received 29 October 2024; Received in revised form 7 January 2025; Accepted 6 February 2025
Available online 7 February 2025

Opalinus Clay, where the short-term undrained rock mass response causes pore pressure changes that may only dissipate over decades (Masset, 2006; Wild and Amann, 2018b). For a reliable prediction of long-term deformation, it is therefore of foremost relevance to understand the material's ability to creep and quantify the rheological creep properties of the rock from targeted and unambiguous laboratory experiments. This can be accomplished through experiments conducted under fully drained loading conditions while maintaining constant effective stresses throughout the creep stages, thereby avoiding deformation caused by pore pressure alterations (i.e., consolidation).

Many studies have investigated the general time-dependent (creep and consolidation) deformation behavior of shales and other clayey rocks with focus on the influence of both intrinsic and extrinsic factors on the rock's physical long-term behavior (e.g., Aristorenas, 1992; Einstein, 2000; Fabre and Pellet, 2006; Naumann et al., 2007; C.L. Zhang, 2013; Sone and Zoback, 2014; Ferrari et al., 2016; Herrmann et al., 2020; Geng et al., 2021; Yu et al., 2023). However, only limited laboratory data exists that effectively distinguish drained creep deformation from consolidation in fully saturated low permeability clay shales (Aristorenas, 1992; Yu et al., 2023). Research specifically addressing the drained creep behavior and the effective long-term strength of saturated shaly Opalinus Clay is particularly scarce (Aristorenas, 1992). Creep studies often ignore poromechanical effects, i.e., consolidation, by testing dried or only partially saturated samples. However, the saturation state affects the creep behavior of clayey rocks since less creep strain is accumulated and creep rates are decreased at lower saturation degrees (Sone and Zoback, 2014; C.L. Zhang and Laurich, 2020). Thus, testing partially saturated rock specimens leads to an underestimation of creep over time. Tests on saturated samples, on the other side, were often conducted with instantaneous (undrained) stress increases, resulting in the superposition of creep deformation and consolidation due to pore pressure alterations (e.g., C.L. Zhang and Laurich, 2020; Yu et al., 2015). Moreover, creep failure has rarely been investigated under controlled pore pressure conditions with established effective stresses (Yu et al., 2023). In order to reliably characterize and quantify creep properties at precisely defined effective stresses, potential pore pressure alterations must be excluded when testing saturated samples.

This experimental study carefully addresses the prerequisites for creep testing of low permeability rock specimens by ensuring both full saturation and the absence of excess pore water pressure to maintain precise effective stress conditions. Tests were conducted to investigate the creep behavior of shaly Opalinus Clay under effective confinement stresses of 4 MPa. Fully drained multi-stage tests with creep stages of each constant effective stress were performed to characterize the pure rheological creep behavior by comparing strain developments at different mean effective stress conditions and differential loading paths to derive creep strain rates as a function of differential stress. In addition, the creep failure observed in the laboratory as well as a potential long-term strength is discussed in the context of dominant creep mechanisms.

2. Materials and methods

2.1. Material description and sampling

Opalinus Clay (OPA) is a middle Jurassic formation with favorable key properties for the isolation of radioactive waste, including its very low permeabilities ($\sim 10^{-21}$ m^2), radionuclide retention capabilities, and self-sealing properties (Bossart et al., 2017). The OPA is classified as a clay shale, exhibiting a transition in properties between a soft rock and a hard soil (Amann et al., 2017). Its properties combine the strength and brittle fracture characteristics known in rock mechanics with the time-dependent and pore pressure-sensitive deformation behavior known in soil mechanics.

The sample material used in this study originates from the Mont Terri Underground Rock Laboratory (MT URL) in Switzerland. The OPA was initially deposited under shallow-marine environmental conditions and buried to depths reaching 1350 m, during the alpine orogeny (Lauper et al., 2021; Mazurek et al., 2006). Uplift and erosion lead to the current depth of the MT URL of 230 to 320 m below the surface, creating an over-consolidated state of the clay shale (Mazurek et al., 2006). The formation is categorized into three distinctive lithofacies, distinguished by variations in the mineralogical composition and the structural facies resulting from changes in the depositional environment (Lauper et al., 2021). For this study, the shaly facies was selected which is characterized by a dark-grey, macroscopically homogeneous fabric with high proportions of clay minerals (56–70 %; Lauper et al., 2021).

The shaly OPA shows a distinct transversely isotropic behavior, resulting from the preferred orientation of minerals and pores along the bedding direction. In the present study, only specimens with the bedding orientation parallel to the maximum loading axis were tested (P-sample configuration). The hydraulic conductivity parallel to the bedding is approximately 10^{-12} m/s (Marschall et al., 2003) with laboratory permeability coefficients of 7.5×10^{-21} m^2 (Winhausen et al., 2021). Porosity measurements yielded values of 15–19 % (Pearson et al., 2003; Wild et al., 2015).

The sample material was obtained by triple-tube-core-barrel drilling with pressurized air-flushing to obtain high-quality core material. The cores (obtained from borehole B-HM-C1) were hermetically sealed in vacuum-evacuated foil immediately after core extraction. Three macroscopically homogeneous cylindrical specimens (OPA1, OPA2, OPA10) were prepared for testing, with dimensions of 60 mm in length and 30 mm in diameter. Additionally, X-ray diffraction analysis (XRD) was carried out on subsamples of the specimens (i.e., end pieces from specimen trimming) to determine the bulk mineralogical composition. The Rietveld quantification method was used, adding a corundum standard, to identify individual mineralogical constituents and to differentiate clay minerals (Moore and Reynolds, 1989; Środoń, 1980).

2.2. Experimental setup

The tests were performed using a triaxial cell with a servo-controlled loading frame and a hydrostatic pressure vessel (Fig. 1a and Fig. 1b). Two spindle pumps regulate the confining pressure (oil medium) and the pore pressure (pore fluid medium). The specimen is jacketed by a rubber sleeve (NBR - nitrile butadiene rubber). Porous plates (stainless steel) are placed at both ends enabling a uniform pore pressure distribution along the specimen's end faces and drained testing conditions. Pore fluid with similar chemical composition to that of the in-situ formation water of OPA from MT was used to minimize chemical alterations of the sample material during testing (based on recipe by Mäder, 2011). Two pressure sensors are connected to the fluid outlets (top and bottom) to monitor fluid pressure changes. The tests are performed at a constant temperature of 30 °C which is monitored by a temperature sensor inside the pressure vessel. Three axial LVDTs (linear variable differential transformers) and a radial extensometer, with resolutions of 20 and 200 nm, respectively, are installed in direct contact with the specimen. Here, the extensometer is positioned perpendicular to the bedding orientation. Furthermore, an additional inner load cell with a resolution of 0.12 N records the applied differential force on the specimen to exclude frictional effects of the piston and the compliance of the testing system. This enables precise and constant differential loading of the specimen.

2.3. Experimental procedure

Prior to testing, a sequence of re-saturation, checks for the Skempton's B coefficient (i.e., B-checks, Skempton, 1954), and consolidation was conducted following a slightly modified procedure of Winhausen et al. (2022) (Fig. 2a).

Re-saturation of the specimen started with a hydrostatic total confining stress (σ_c) of 1.5 MPa and a back-pressure (controlled pore

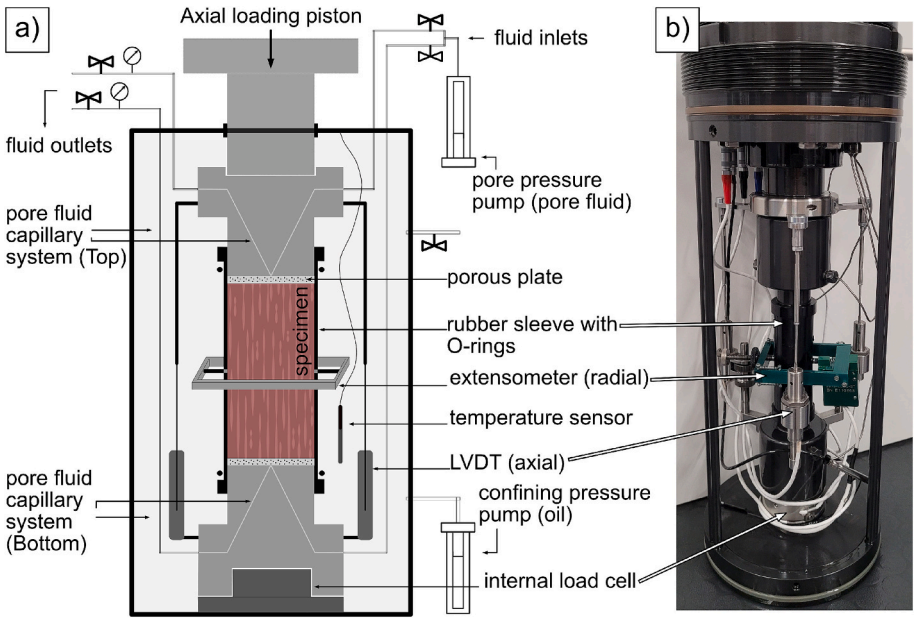

Fig. 1. a) Schematic and b) photography of the experimental setup.

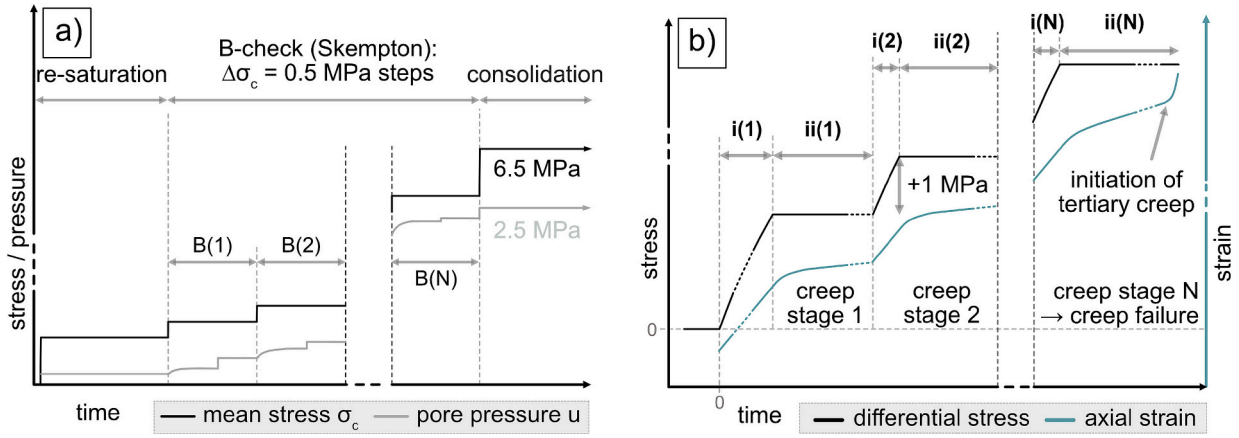

Fig. 2. *Schematic representation of the pre-test saturation and consolidation of the specimen, and the multistage creep test protocol. a) The stress/pressure history of the hydrostatic confining stress (σ_c) and the pore pressure (u) during the sequence of re-saturation, B-check phase for saturation verification, and consolidation of the fully saturated specimen at the target stress state of σ_c= 6.5 MPa and u = 2.5 MPa; b) Differential stress ($q = \sigma_1 - \sigma_3$) loading path and theoretical axial strain curve during a multi-stage test with i(n) drained axial stress increments, followed by ii(n) constant effective stress creep stages.*

pressure at specimens' end faces) of 0.3 MPa, establishing an effective stress state of 1.2 MPa (Fig. 2a). During the B-check phase, Skempton's (B) coefficients (Eq. 1) were determined to verify the saturation state of the sample, under the assumption of Terzaghi's effective stress principle and the incompressibility of the pore fluid.

$$B = \frac{\Delta u}{\Delta \sigma_c} \tag{1}$$

For each B-check (Fig. 2a), the hydrostatic confining stress was increased by 0.5 MPa ($\Delta\sigma_c$) under undrained conditions whilst the change in pore pressure (Δu) was measured. After each B-check, the back-pressure was increased to re-establish the initial effective stress state of 1.2 MPa. Skempton's B coefficient equals one for a fully saturated isotropic elastic porous medium (Skempton, 1954). However, as demonstrated by Wild et al. (2017) and Winhausen et al. (2022), Skempton's B may be smaller than unity for Opalinus Clay. The procedure was repeated until the specimen was verified fully saturated by obtaining two subsequent B-checks with $\Delta B \leq 0.05$ or $B \geq 0.95$.

After re-establishing full saturation, all specimens were consolidated at an effective confining stress of 4 MPa (i.e., $\sigma_c = 6.5\,MPa; u = 2.5\,MPa$; Fig. 2a). The consolidation was considered complete when no further excess pore water pressure dissipated and the theoretical degree of full consolidation was reached, following the curve-fitting method (log-time) after Casagrande (Casagrande and Fadum, 1940). Theoretical full consolidation was achieved when the consolidation curve changed from non-linear (primary consolidation) to linear (secondary compression) in a semi-logarithmic plot (log-time). This transition was identified by the intersection of two semi-logarithmic tangents. One of these was located at the inflection point of the non-linear part of the consolidation curve, while the other represented the backward extrapolation of the linear part of the consolidation curve (Head and Epps, 2011). The consolidation curves are provided in the digital appendix (Appendix - Fig. A1). The hydrostatic effective confinement applied during consolidation was maintained for subsequent testing ($\sigma'_c = 4\,MPa$).

The multi-stage creep tests were comprised of an alternating sequence of two distinct phases i(n) and ii(n) (Fig. 2b). The first phase i (n) involved the application of differential stress increments under drained conditions by increases in the axial stress. This was followed by

the second phase ii(n) involving the application of constant effective stresses, i.e., the creep stages. Fig. 2b schematically shows the differential ($q = \sigma_1 - \sigma_3$) multi-stage loading path and a theoretical axial strain response typical for creep tests. In this study, positive strain was defined as compression, whereas negative strain was denoted as extensional deformation.

This study presents two multi-stage creep tests with different loading paths, i.e., differential stress path, on two specimens labeled as OPA1 and OPA2. The initial differential stress increment (Fig. 2b - i(1)) was selected to be q = 2 MPa for specimen OPA1, and q = 12 MPa for specimen OPA2, with uniform differential stress increases of 1 MPa between each subsequent creep stage. The initial creep stage for specimen OPA2 was chosen to be close to the creep failure stress conditions obtained from specimen OPA1. The primary objective, here, was to study the impact of accumulated strain on creep strain rates and creep failure associated with a different multi-stage loading path.

The drained stress increments (Fig. 2b – i(n)) were performed under axial strain-controlled conditions resulting in a non-linear increase of the axial load. To prevent any built-up of excess pore pressure, appropriately slow strain rates were determined based on specimen-specific consolidation coefficients (Bishop and Henkel, 1962; Head, 1998). The consolidation coefficient (c_v) was calculated based on the drainage length of the specimen ($h = 30\ mm$) and the elapsed time for complete consolidation ($t_{100}\ in\ s$) following the (log-time) method after Casagrande (Eq. 2) (Bishop and Henkel, 1962).

$$c_v = \frac{\pi h^2}{4t_{100}} \tag{2}$$

For determining the time to failure (t_f) (Eq. 3) a drainage coefficient of $\eta = 3$ was assumed due to pore fluid drainage at both of the specimen's end faces (Bishop and Henkel, 1962):

$$t_f = \frac{20h^2}{\eta c_v} \tag{3}$$

The axial strain rate for shearing ($\dot{\varepsilon} = \varepsilon_f / t_f$) was calculated assuming an axial strain at failure of 0.5 %. Similar axial failure strains have been observed for P-samples from consolidated drained (Favero et al., 2018) and undrained (Wild and Amann, 2018a; Winhausen et al., 2022) triaxial short-term compression tests on shaly Opalinus Clay. For specimens OPA1 and OPA2, consolidation coefficients (c_v) of 0.023 and 0.013 mm^2/s, respectively, were determined which result in axial strain rates for shearing of $2 \times 10^{-8}\ s^{-1}$ and $1 \times 10^{-8}\ s^{-1}$.

For each stress increase (Fig. 2b – i(n)), the drained stress-strain relationship, here referred to as tangent modulus ($E_T = \Delta\sigma/\Delta\varepsilon$), was determined. The slope was calculated by a linear least-square regression within a predefined strain interval at the start of each differential stress increase (0.0 % ≤ Δε ≤ 0.01 %; Fig. 3).

The individual creep stages (Fig. 2b – ii(n)) were performed under constant effective stress conditions and maintained until the axial strain rates reached quasi-steady state conditions. The quasi-steady state was considered to be reached when an appropriate linear approximation ($R^2 \geq 0.998$) of the strain curve was obtained for a representative time interval of more than 6 days. Studies on comparable shales indicate that the steady-state conditions were reached after 10 to 20 days, which remained constant even after years of creep testing (Gasc-Barbier et al., 2004; Yu et al., 2015). In the course of the present study, similar time periods were observed, during which the change in creep rates was found to be negligible small. Axial and radial secondary creep rates were determined by the slope of a linear regression within the quasi-steady state time interval. After each creep stage, the differential stress was increased further (steps of Δq = 1 MPa, Fig. 2b), until creep failure could be identified as an exponential acceleration of the axial strain rate. Finally, the specimen was unloaded and dried in an oven at 105 °C to measure the water content.

An additional drained short-term test (labeled as OPA10) was conducted to obtain the reference short-term strength of the same OPA facies under identical boundary conditions (i.e., effective consolidation stress, temperature, saturation state). The specimen was saturated and consolidated using the same protocol and subsequently sheared under drained conditions with a constant compression rate of $1 \times 10^{-8}\ s^{-1}$ ($c_v = 0.020\ mm^2/s$) beyond peak stress until constant residual differential stress.

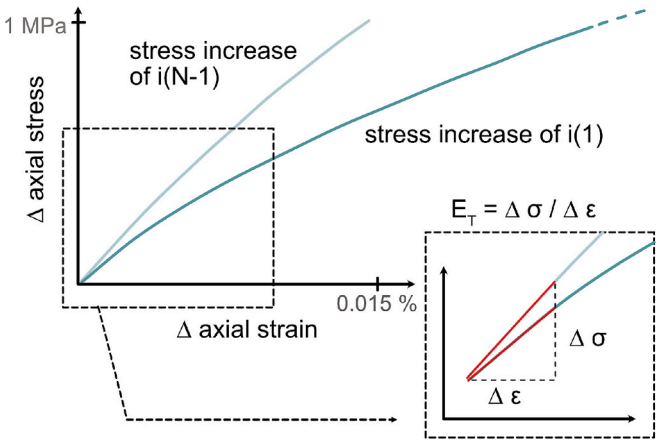

Fig. 3. Exemplary stress-strain curves of the first i(1) and the second to last i(N-1) stress increase are displayed to show how the tangent modulus was determined from a consistent strain interval (0.0 % ≤ Δε ≤ 0.01 %) at the beginning of each stress increase.

3. Results

The X-ray diffraction analysis of this study showed that the specimens used for creep testing (OPA1 and OPA2) had a similar mineralogical composition, primarily consisting of clay minerals (~70 wt%) such as illite, chlorite, kaolinite, and illite-smectite mixed layers. Other constituents of the mineralogical composition were approximately 10 wt % quartz, 15 wt% carbonates, and 4 wt% other minerals (e.g., feldspar, pyrite, rutile). The homogeneous mineralogy allowed a representative comparison between both specimens. In contrast, the reference specimen OPA10 exhibited a slightly reduced proportion of clay minerals (~58 wt%) and a larger proportion of carbonates (~25 wt%), but this composition still falls into the typical range of the shaly facies. Table 1 lists the detailed mineralogical compositions of the three specimens. Further data of the XRD-analyses, used for the determination of the mineralogy, are provided in the digital appendix (Appendix – Fig. A2).

The post-experimental determination of the water content yielded values of 8.09, 8.34, and 7.19 % for specimens OPA1, OPA2, and OPA10, respectively. Relative to their pre-test conditions, all specimens represented an increase in water content of 1.02, 1.61, and 1.24 % for specimens OPA1, OPA2, and OPA10, respectively.

Table 1
Mineralogical composition of the tested specimens OPA1, OPA2 and OPA10 from XRD-analysis performed in this study.

Mineralogy	OPA1 [wt%] Long-term	OPA2 [wt%] Long-term	OPA10 [wt%] Short-term
Clay minerals	70.7	69.3	57.5
(chlorite, kaolinite)	(25.9)	(24.2)	(22.1)
(illite, illite/smectite mixed layers)	(44.8)	(45.1)	(35.4)
Quartz	10.2	10.6	10.4
Carbonates	14.4	15.8	24.5
Others	4.8 (3.5; 0.9;	4.4 (3.5; 0.7;	7.6 (6.6; 1.0;
(feldspar; pyrite; rutile)	0.4)	0.2)	0.0)

3.1. Creep testing

Two creep tests (OPA1 and OAP2) with different multi-stage loading paths were conducted at an effective confinement of 4 MPa. In the multi-stage creep test of specimen OPA1, the differential stress was initially increased to 2 MPa, followed by 11 increments of 1 MPa each, reaching a final differential stress of 13 MPa (Fig. 4a). The duration of the individual creep stages from $q = 2$ MPa to $q = 12$ MPa ranged from 13 to 22 days. The final creep stage (q = 13 MPa), however, lasted 6.3 h due to the rapid onset of tertiary creep, leading to creep failure. The total duration of the first creep test was 192 days (Fig. 4a). In the second multi-stage creep test (OPA2), four creep stages were performed with constant loading at differential stresses from $q = 12$ MPa to $q = 15$ MPa, applied in 1 MPa increments (Fig. 4a). The creep stages in this test lasted from 13.5 to 21 days, which was similar to the first test. The final creep stage (q = 15 MPa) lasted 13.5 days before the onset of tertiary creep. Due to the modified multi-stage loading path, the total duration of the second creep test was 74 days (Fig. 4a). Fig. 4b shows post-experimental cross-sections of specimen OPA1 and OPA2, which indicate a distinct shear failure resulting from creep failure.

For comparison between the short-term strength and the long-term strength a conventional short-term compression test was conducted as a reference test (OPA10). Specimen OPA10 exhibited short-term peak strength at a differential stress of 14.5 MPa after 8.5 days of shearing (Fig. 5a). The residual strength was subsequently reached at approximately 7.3 MPa. Fig. 5b shows a post-experimental cross-section of specimen OPA10, which indicates two distinct failure planes resulting from shear failure.

Fig. 4a illustrates the axial and radial strains as functions of time for both multi-stage creep tests. To enable direct comparison of the multi-stage tests, the strains accumulated during saturation and consolidation were reset to zero. The axial strain curves in both tests exhibited a continuous compressive deformation behavior throughout all stress increases and the creep stages (Fig. 4a). The radial strain curve, however, exhibited a more complex behavior, showing both compressive and extensive deformations during creep stages (Fig. 4a).

The individual differential stress increases (Fig. 2b – i(n)) in the multi-stage tests as well as the loading of the reference test showed a typical loading response with axial compression and radial extension (Fig. 4a and Fig. 5a). The stress-strain curves showed a short linear behavior, transitioning to non-linear responses indicative of stiffness degradation. A comparison of the radial stress-strain curves of specimen

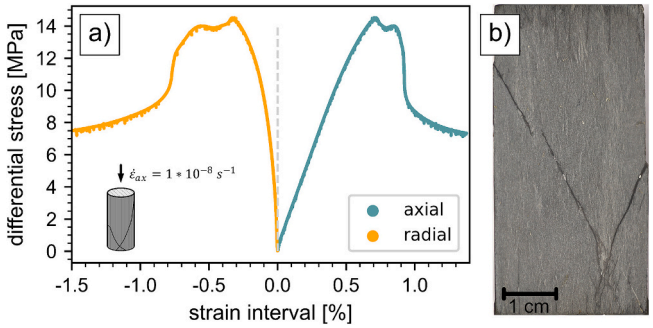

Fig. 5. *a) Stress-strain curves of the short-term reference test OPA10 with a peak strength of $q = 14.5$ MPa at an effective confining stress of 4 MPa* (i.e., $\sigma_c = 6.5$ *MPa*; $u = 2.5$ *MPa*). *b) Cross-section of specimen OPA10 after failure.*

OPA2 (i(1) from q = 0 MPa to q = 12 MPa) and specimen OPA10 (i(1) from q = 0 MPa to q = 14.5 MPa) revealed a discrepancy in the onset of non-linearity, i.e., the onset of yielding. For specimen OPA2, the onset of yielding occurred at a differential stress between $q = 4$ and 5.5 MPa (Fig. 6). In contrast, for specimen OPA10, the onset of yielding occurred

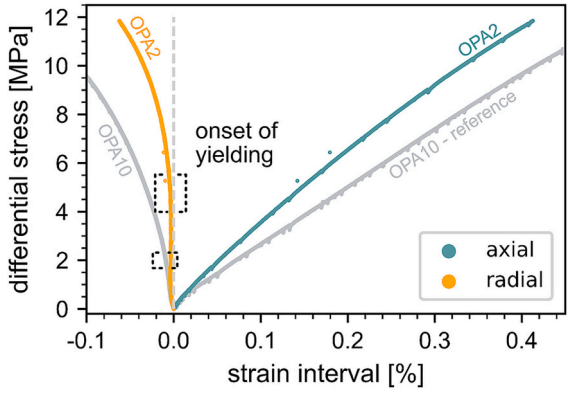

Fig. 6. Stress–strain curves for the initial differential loading of OPA2 from hydrostatic conditions to q = 12 MPa and the differential loading curve of the reference test (OPA10) resulting from an axial compression rate of 1×10^{-8} s^{-1} for both tests.

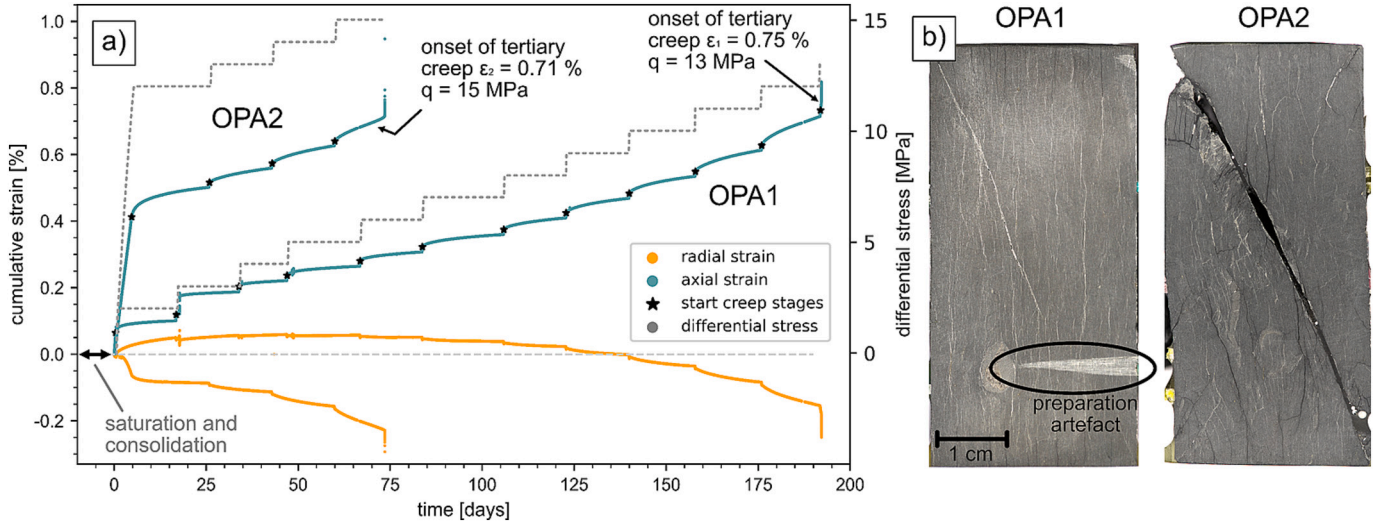

Fig. 4. *a) Cumulative axial and radial strains throughout the multi-stage creep tests for OPA1 and OPA2 as well as the differential stress paths at an effective confining stress of 4 MPa* (i.e., $\sigma_c = 6.5$ *MPa*; $u = 2.5$ *MPa*). *The geomechanics convention is used with negative values for extension and positive values for compression. b) Cross-sections of specimens OPA1 and OPA2 after creep failure indicating failure planes.*

when the differential stress exceeded 2 MPa (Fig. 6).

For the reference test OPA10, an initial tangent modulus of 4.1 GPa was determined by the linear response (Fig. 7). With further shearing, a non-linear stress-strain relationship could be observed until failure, representing continuous stiffness degradation (Fig. 5a). In contrast, specimens OPA1 and OPA2 indicated a recovery in stiffness subsequent to each creep stage, as evidenced by increases in the tangent modulus (E_T, Fig. 7). Specimen OPA1 exhibited a progressive increase of E_T from 4.8 to 7.1 GPa at differential stresses from 2 to 6 MPa (Fig. 7). At differential stresses exceeding 7 MPa, E_T stabilized, averaging to approximately 7.4 GPa. During the final differential stress increase ($12 \leq q \leq 13$ MPa), E_T decreased to 6.8 GPa, accompanied by greater non-linearity of the stress-strain curve compared with previous stress increases. Specimen OPA2 exhibited an increase of E_T from initially 4.8 to 7.8 GPa after the first creep stage and finally stabilized to a nearly constant value of 7.8 GPa in subsequent stress increases (Fig. 7).

Fig. 8 shows the strain curves, i.e., creep curves, which were observed during the creep stages (Fig. 2b – ii(n)). Each creep curve was segmented into two to three sections based on the development of strain over time, i.e., strain rate, and, accordingly, associated with one of three creep phases. Decelerating strain rates after differential stress increases were interpreted as (1) primary creep, quasi-steady-state strain rates were interpreted as (2) secondary creep, and accelerating strain rates were interpreted as (3) tertiary creep. Primary and secondary creep was observed in almost all applied creep stages, whereas tertiary creep occurred only in later stages and led to creep failure of the specimens ($q = 13$ MPa for OPA1 and $q = 15$ MPa for OPA2; Fig. 8). As the differential stress stages increased, the amount of axial shortening resulting from primary creep showed a gradual increase across successive creep stages (Fig. 8a and Fig. 8c). The radial strain curve indicated a more complex behavior (Fig. 8b and Fig. 8d). The beginning of constant effective stress stages led to an immediate radial compression which was attributed to primary creep deformation. Under maintained constant load, the radial strain curve showed either sustained compression (primary and secondary creep) at low differential stress ($2 \leq q \leq 5$ MPa) or a transition from initial compression to extension within a few hours, which ultimately led to an extensional secondary creep behavior ($q \geq 6$ MPa). However, in specific creep stages, including the final stress stages and the initial creep stage of specimen OPA2, the radial strain curve indicated an immediate extension without any compressive response.

Both the axial and radial strain curves as well as the axial strain rate evolution of the final creep stage of specimen OPA1 (q = 13 MPa) is illustrated in more detail in Fig. 9. During this final creep stage, no primary creep response could be observed. Instead, secondary creep was characterized by a relatively short (~ 4.5 h) axial (compressive) and radial (extensional) response, which was followed by tertiary creep. Prior to initiation of tertiary creep, the minimum strain rate was determined to be 9.86×10^{-9} s^{-1} (Fig. 9). The total cumulative axial strain was found to be approximately 0.75 % at the onset of tertiary creep (Fig. 4a).

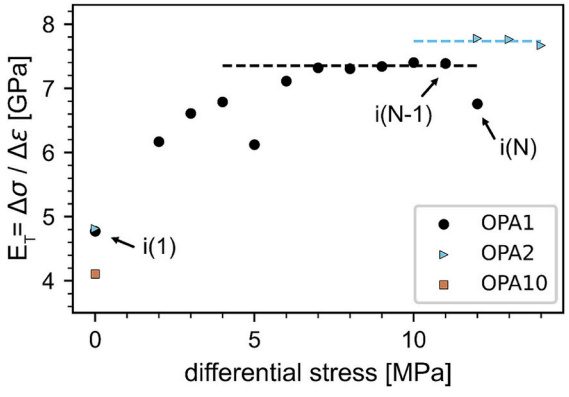

Fig. 7. *Drained tangent moduli (E_T-module) of the individual stress* increases *(at $\sigma_c' = 4$ MPa).*

In contrast, the strain curves of the final creep stage of specimen OPA2 exhibited a primary creep phase that transitioned into secondary creep behavior for both axial and radial directions (Fig. 8c and Fig. 8d). Prior to initiation of tertiary creep, the minimum strain rate was determined to be 4.91×10^{-10} s^{-1}. After 300 h of constant differential stress (q = 15 MPa), the specimen exhibited strain rate acceleration, resulting in creep failure. The total cumulative axial strain was found to be approximately 0.71 % at the onset of tertiary creep (Fig. 4a). It is important to note that the creep phases do not represent sharp boundaries but rather a gradual transition.

3.2. Secondary creep strain rates

Fig. 10 illustrates the axial and radial creep strain rates during the secondary creep deformation (2) of each differential stress stage. The magnitudes of the strain rates fall within the range of 10^{-11} to 10^{-9} s^{-1}.

The results of both multi-stage tests demonstrated an increase in the axial secondary creep rates with increasing differential stress (Fig. 10). In the low differential stress regime ($2 \leq q < 10$ MPa), specimen OPA1 showed minor strain rate changes in the range of 7×10^{-11} s^{-1}. With increasing differential stress (≥ 10 MPa), the axial strain rates increased exponentially. In contrast, the radial secondary creep rates of specimen OPA1 exhibited first a transition from compression ($q \leq 5$ MPa) to extension ($q \geq 6$ MPa). Subsequently, these radial strain rates showed an exponential trend towards negative strain rate values, i.e., extension, under high differential stresses (≥ 10 MPa). The comparison of strain rates of the two multi-stage tests indicated an identical trend at high differential stresses, however, a 3 MPa shift along the differential stress axis (Fig. 10). For instance, similar axial strain rates of 1.61×10^{-10} s^{-1} and 1.64×10^{-10} s^{-1} were observed at different stress stages ($q = 9$ MPa and $q = 12$ MPa for OPA1 and OPA2; Fig. 10).

4. Discussion

The following sections discuss the main observations that are relevant for the description of the constitutive creep behavior of shaly OPA. The analysis of the laboratory data aims to understand the macro- and micro-mechanical processes of creep deformation and to quantify creep behavior under fully drained and fully saturated in situ conditions.

The following analysis is based on a comparison between the three tests performed, i.e., two multi-stage creep tests and a reference short-term test. The specimens' discreetness and variability are considered negligible, as Minardi et al. (2021) demonstrated a high degree of reproducibility of the short-term deformation behavior in a triaxial testing benchmark study on shaly OPA. Based on the homogeneous mineralogy of the used specimens (Table 1) with similar physical properties (e.g., E_T of initial loading, Fig. 6) a direct comparison of the two different multi-stage loading paths is considered feasible. Although, specimen OPA10 slightly deviates in the mineralogy and the physical properties, the results are still within the broader characterization range of the shaly facies of OPA. Therefore, the analysis and conclusions drawn are inferred to be valid.

4.1. Onset of yielding and volumetric dilation

The transition from linear to non-linear behavior in the stress-strain curves during constant axial compression indicates the onset of yielding, i.e., irreversible deformation due to initiation of microcracking, and was determined from the radial strain curve. As illustrated in Fig. 6, the reference test (OPA10) shows an early onset of yielding at a differential stress of approximately 2 MPa. This transition corresponded to 14 % of the short-term peak strength ($q_{peak,OPA10} = 14.5$ MPa, $\sigma_c' = 4$ *MPa*). However, the onset of yielding for OPA2 could be estimated at a slightly

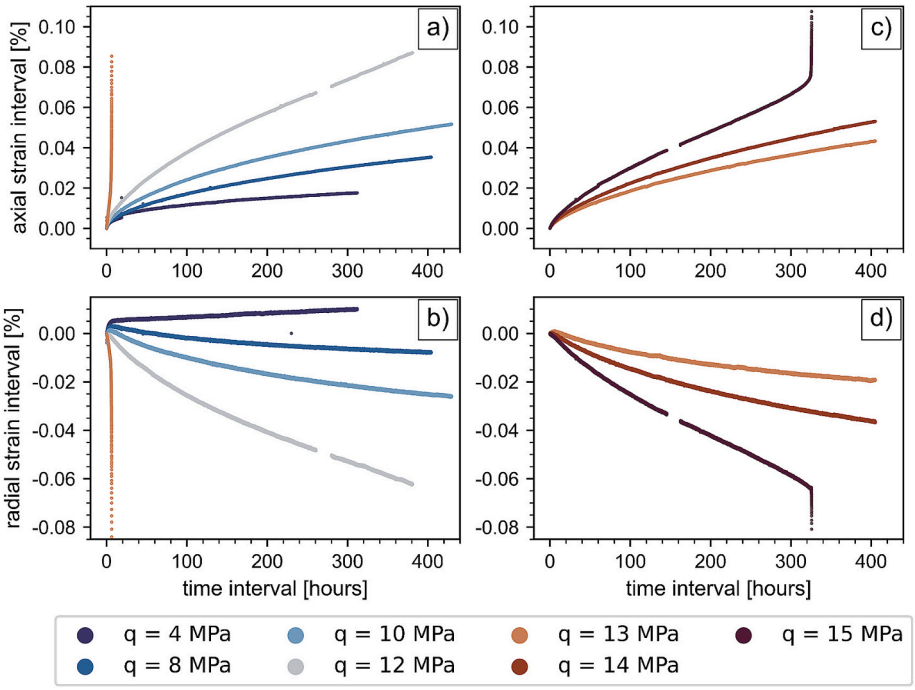

Fig. 8. Representative a) axial and b) radial strain curves ii(n) of individual selected creep stages (q = 4, 8, 10, 12, 13 MPa) in test OPA1; c) axial and d) radial strain curves ii(n) of individual selected creep stages (q = 13, 14, 15 MPa) in test OPA2.

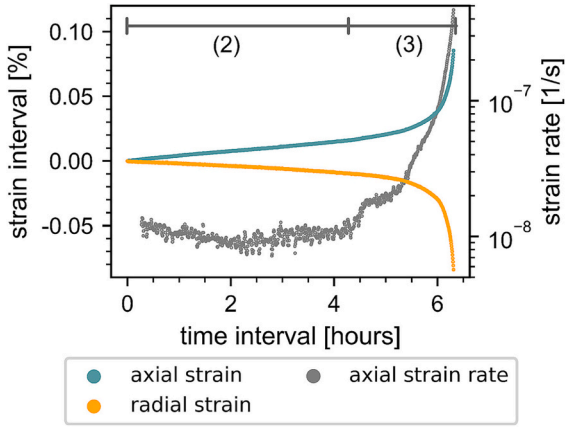

Fig. 9. Axial and radial strain as well as the axial strain rate as a function of time for the final creep stage of OPA1 with constant axial load of q = 13 MPa. The creep phases are indicated by (2) secondary creep and (3) tertiary creep.

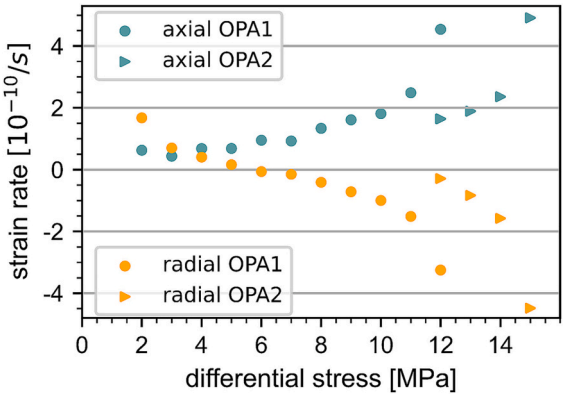

Fig. 10. Axial and radial secondary creep rates (2) obtained from the individual stress stages during the multi-stage creep testing of OPA1 (dots) and OPA2 (triangles).

higher differential stress of approximately 4 to 5.5 MPa which ranged between 26 % and 38 % of the short-term peak strength (Fig. 6). Due to identical experimental boundary conditions and the same axial compression rate, the discrepancy can only be attributed to differences in the stiffness of the material, showing slightly weaker properties for specimen OPA10, i.e., lower E_T and stronger stiffness degradation (Fig. 6 and Fig. 7). This discrepancy is considered to fall within the natural sample variability.

With the onset of yielding, the rate of volumetric compression decreases until eventually changing into net dilation, i.e., dilation boundary (Bieniawski, 1967). The creep curves of the multi-stage tests demonstrate a comparable development of overall creep compaction, which is relatively decreasing with increasing differential stress. For specimen OPA1, the axial and radial strains suggest the presence of strong compressive creep deformation up to at least 5 MPa of differential stress (Fig. 10). Under differential stresses which are exceeding 5 MPa, the radial creep strain changed from compressional to extensional, indicating a dominant reduction in volumetric compaction. This change in the radial creep direction, perpendicular to the bedding, coincides with the onset of yielding from OPA2 and can be associated with plastic creep deformation due to the initiation of micro-cracking. In this study, the ultimate transition from volumetric creep compaction to net creep dilation could not be determined due to the one-dimensional measurement of radial deformation. Nevertheless, studies on various argillaceous sedimentary rocks revealed a similar development of creep compaction under low differential stresses, whereas increased differential stresses resulted in dilation when approaching long-term failure conditions (Fabre and Pellet, 2006; Geng et al., 2018).

4.2. *Secondary creep and creep mechanisms*

In all performed creep stages except for one, primary and secondary creep was identified in both axial and radial direction (Fig. 8), even at

differential stress levels below the onset of yielding. Therefore, no lower stress threshold for secondary creep was identified for fully saturated shaly OPA under an effective confining stress of 4 MPa. Common stress conditions under which the transition from primary to secondary creep occurs in shales remain debated and scholars state opposing conclusions on the existence of a lower stress threshold of secondary creep. Some authors describe ongoing attenuation of creep below a certain stress level (Fabre and Pellet, 2006; Rybacki et al., 2017; Yu et al., 2023), while others have observed very small secondary creep rates even at very low differential stresses or at hydrostatic stress conditions (C.L. Zhang, 2013; C.L. Zhang and Laurich, 2020). These latter studies agree with the observations of the present study and suggest that no threshold for secondary creep exists.

Creep rates in clay-rich low permeability rocks are often reported down to 10^{-12} or 10^{-11} s^{-1}, which is close to the typical resolution of displacement sensors (Fabre and Pellet, 2006; Yu et al., 2015; C.L. Zhang and Laurich, 2020). Whether reported values indicate actual attenuation of creep over time or simply a drop below the sensor detection limit remains unclear and may explain opposing results. In this study, low differential stresses of q = 2 MPa yielded extremely low yet persistent strain rates. Axial strain rates down to 10^{-11} s^{-1} were observed which correspond to displacement rates of approximately 10 nm per hour. The displacement sensors used in this study, provide a resolution of 20 nm, which does not allow a reliable analysis of the lowest creep rates within time intervals below two hours. However, the presented secondary creep strain rates were based on 150 h intervals during which accumulated strain could be resolved and used to calculate the strain rates. For higher creep stages, the strain rates were closer to or within the resolution of these sensors even at smaller time intervals. Therefore, the resolution of the displacement sensors is considered adequate to capture secondary creep deformation.

The observed secondary strain rates exhibited an exponential increase with increasing differential stress (Fig. 10). This finding is consistent with other creep studies, where secondary creep was identified (C. L. Zhang, 2013; C.L. Zhang and Laurich, 2020; Geng et al., 2018, 2021; Naumann et al., 2007). However, the absolute creep strain rates determined are five to ten times higher than those reported in other studies on shaly Opalinus Clay (Gräsle and Plischke, 2010; C.L. Zhang, 2013; C.L. Zhang and Laurich, 2020). This discrepancy can be attributed to differences in the effective stress and the saturation state. Accordingly, specimens with a decreased saturation degree yield an increased total strength as demonstrated by conventional short-term compression tests. This is due to suction pressures within the pores which change the actual effective stress conditions (Wild et al., 2015). This phenomenon can lead to an overestimation of both stiffness and effective short-term and long-term strength compared to fully saturated specimens. The internal suction pressure is also expected to affect the creep behavior of shales as evidenced by decreased creep strain rates from clay shale specimens of decreased saturation (C.L. Zhang and Laurich, 2020; H. Wang et al., 2023). This causes an underestimation of the creep deformation and the long-term strength.

The exponential trend of increasing secondary creep rates with increasing differential stress (Fig. 10 - OPA1) allows for a subdivision into two separate creep regimes: (a) stress-insensitive and (b) stress-sensitive behavior associated with distinct deformation processes. In the low-stress regime, stress-insensitive secondary creep prevails, indicated by only minor strain rate changes. In contrast, larger strain-rate changes at high differential stresses are associated with stress-sensitive mechanisms. For an effective confinement of 4 MPa, the threshold dividing these regimes is approximately 10 MPa differential stress (mean effective stress of 7.3 MPa).

According to the simplified power-law creep model by Norton (Norton, 1929; Golan et al., 1996), the secondary creep rates can be expressed as power law functions of the differential stress (Eq. 4).

$$\dot{\varepsilon} = A^{*}\sigma^{n} \tag{4}$$

Where $\dot{\varepsilon}$ (s^{-1}) is the secondary creep rate, σ is the applied (von Mises) stress, here referred to as the differential stress q (MPa), and n (−) is the power law exponent. The power law exponent represents the sensitivity of strain-rates to the stress state $\left(n = \frac{\partial log(\dot{\varepsilon})}{\partial log(\sigma)}\right)$, which serves as an indicator for characteristic creep mechanisms (Dusseault and Fordham, 1993). The coefficient A is a pre-exponential term consisting of the material constant C (MPa^{-n}/s), the specific (mechanism-dependent) activation energy Q (J/mol), the gas constant R (8.32 J/K/mol), and the temperature T (303.15 K = 30 °C) (Eq. 5).

$$A = C^{*}exp^{\left(\frac{-Q}{RT}\right)} \tag{5}$$

In the low-stress regime ($2 \leq q \leq 10$ MPa) of specimen OPA1, the regression analysis of the strain rates as a function of the differential stress yielded a power law exponent of 0.8 indicating stress-insensitivity (Fig. 11). In contrast, in the high-stress regime ($q \geq 10$ MPa), the regression analysis yielded an increased power law exponent of 5.0 indicating stress-sensitivity (Fig. 11). The distinction between these two power-law exponents is likely associated with a change in the predominant micro-scale creep mechanism when a certain stress threshold is exceeded. However, the boundary is not sharp but rather a transitional range in which the dominating processes gradually change. Although only high differential stress stages ($q \geq 12$ MPa) are applied in the second test (OPA2), in comparison with the first test (OPA1), a similar power law fit with $n = 4.7$ suggests that stress-sensitive creep mechanisms are predominant (Fig. 11).

As shown by a variety of studies on rocks, specific power law exponents are attributed to specific creep mechanisms. An exponent of $n \approx 1$ represents a linear stress vs. strain rate relationship. This relationship is often derived from deformation which is driven by diffusive mass transfer or pressure solution creep (Spiers et al., 1990; Cristescu and Hunsche, 1998; Rybacki and Dresen, 2000). Exponents greater than unity are usually associated with creep deformation by dislocation glide ($n \approx 3$, (Dusseault and Fordham, 1993; Rybacki and Dresen, 2000) or dilatant brittle behavior ($n >> 3$ highly variable, (Atkinson, 1984; Kranz, 1979; Brantut et al., 2012). The brittle regime of creep deformation, including microcracking and eventually shearing, shows a highly stress-sensitive relationship of creep rates. The dominance of micro-cracking indicates a potential for failure over time due to progressive damage accumulation.

Consequently, the creep mechanism which is present in the low stress regime is inferred to be diffusion creep. In the high stress regime, on the other hand, the creep mechanism can be attributed to microcracking, i.e., brittle creep. A similar analysis was proposed by Geng

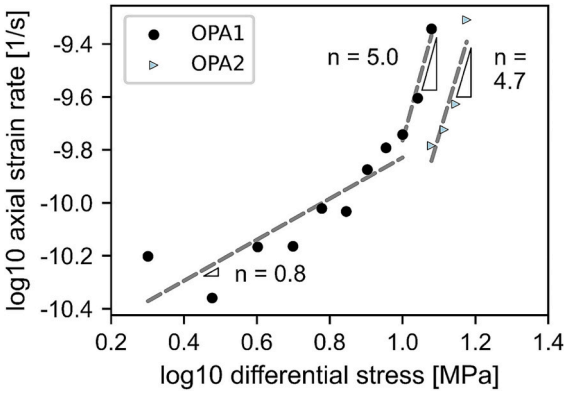

Fig. 11. *Axial secondary creep rates as a function of applied differential stress (at an effective confining stress of 4 MPa) with power law exponent* $\left(n = \frac{\partial log(\dot{\varepsilon})}{\partial log(\sigma)}\right)$ *fits for the low ($q \leq 10$ MPa) and high ($q \geq 10$ MPa) differential stress regime.*

et al. (2018, 2021) based on multi-stage creep tests on Tournemire shale. They suggested that pressure solution creep occurs in the low stress regime, whereas microcracking dominates creep deformation close to creep failure stress conditions.

4.3. Damage and recovery

For the understanding of deformation in multi-stage creep tests, several processes must be considered: 1) accumulated damage during differential stress increases, and 2) damage and recovery processes occurring under constant effective stress, i.e., creep stage. For crystalline rock and rock salt, creep deformation is understood as a balance between these damage and recovery processes (Pusch and Hökmark, 1992; Cristescu and Hunsche, 1998), a concept also possible to be applied to clay-rich rocks (Geng et al., 2018; Yu et al., 2023). The dominance of either damage or recovery during creep is considered to impact the creep rate as well as the failure strength in dependence of stress state and time (Pusch and Hökmark, 1992; Yu et al., 2023).

The accumulation of damage in form of microcracking and crack growth, as the differential stress increases, results in weakening and stiffness degradation throughout the progressive loading. However, for differential stresses up to 7 MPa, an increase in stiffness was observed subsequent to creep accumulation, as shown by the increase in the tangent modulus (E_T, Fig. 7). This observation suggests that creep deformation is primarily governed by recovery processes accompanied by diffusion mass transfer, as suggested by the power law analysis, as well as compaction due to microcrack closure, pore collapse, and particle rearrangement. These processes result in the mechanical interlocking of the clay particles, thereby enhancing the strength and stiffness of the material. For differential stresses exceeding 7 MPa, however, E_T reaches a plateau, which means that the amount of creep recovery processes is no longer able to increase the stiffness of the specimen. Comparable findings were reported by Geng et al. (2018, 2021) from triaxial multi-stage creep tests on Tournemire shale. Their study analyzed the hardening modulus derived from the stress-strain curve, which decreased during the differential stress increases, but significantly recovered and even increased in successive differential loading phases. Finally, this parameter converged towards a constant stress-strain relationship (Geng et al., 2021). In consolidation tests, a similar strengthening of clayey rocks is observed until it reaches a certain hardening level (Yu et al., 2021).

P-wave velocity measurements revealed that the stiffening effects during the secondary creep phases decrease with increasing differential stress, which takes place until the dominant processes are reversed, i.e., recovery-dominated to damage-dominated (Geng et al., 2018; Li et al., 2023). This point of reversal is interpreted to coincide with the previously introduced stress threshold, at which the creep behavior changes from stress-insensitive to stress-sensitive processes (Fig. 11). A reduced dominance of recovery processes and/or pronounced dominance of damage processes leads to stress-sensitive mechanisms represented by the exponential increase of creep strain rates. The change into damage-dominated creep, i.e., brittle creep, was not observed by oedometric long-term deformation tests on clay shales. While in triaxial creep tests the secondary creep rates increase exponentially accompanied by radial extension, oedometer tests show a stabilization of the creep rate when the hardening stabilizes due to the restriction of radial deformation and, thus, the absence of brittle dilation (Ferrari et al., 2016; Yu et al., 2021).

The final stress increase of specimen OPA1 (q = 12 MPa to q = 13 MPa) exhibited enhanced damage accumulation, demonstrated by a reduced E_T (Fig. 7) and a more-pronounced non-linearity of the stress-strain curve. In addition, the specimen did not experience any primary creep. Instead, only a short secondary creep phase occurred, which was followed by tertiary creep leading to creep failure (Fig. 9). This finding suggests that the specimen was already close to failure during the differential stress increase, favored by very high density of unstable fractures, i.e., damage, that continued to propagate and coalesce. In contrast, the final stress increase of the second test (OPA2), did not present an intensified curve flattening, and, subsequent, all three creep phases, i.e., primary, secondary, and tertiary creep, could be identified (Fig. 8c). The critical failure conditions of specimen OPA2 were reached later in the final creep stage, due to progressive accumulation of damage during the secondary creep phase.

Apart from the strain rate dependence on effective stress changes, the actual multi-stage loading path history has also been shown to influence the secondary creep behavior. The comparison of the axial strain rates of identical stress stages (e.g., q = 12 MPa) exhibited higher rates when preceded by several creep stages (Fig. 10). Similar observations were reported by Gasc-Barbier (2004) on OPA, who described divergent creep strain rates at equal stress conditions when comparing mono-stage creep tests and multi-stage creep tests. These observations suggest a correlation between the total cumulative strain accumulation, with either damage or recovery processes, and the absolute strain rates. Accordingly, either less damage was accumulated or more creep recovery occurred in the first creep stage of specimen OPA2. Whether the point of behavior reversal is also shifted must be verified by additional tests using a variety of multi-stage loading paths.

4.4. Short-term strength and long-term strength

Winhausen et al. (2022) established a short-term failure criterion of the shaly OPA based on previous studies performing conventional drained and undrained compression tests. A comparison of the effective short-term strength (q_{peak} = 14.5 MPa) obtained by the drained reference test (OPA10) with this failure criterion reveals a slight deviation from the fitted peak strength at similar effective confining stresses ($q_{peak\text{-}fit} \approx$ 16 MPa; intersection of failure criterion and drained stress path in Fig. 12). Nevertheless, the peak strength of OPA10 is still within the confidence interval (95 %) and reflects the natural variability of the laboratory results. Thus, the performed reference test and the experimental setup is considered representative of the short-term deformation behavior of shaly OPA.

The creep-tested specimens developed creep failure at 90 % (OPA1) and 103 % (OPA2) of the short-term peak strength (OPA10) at similar effective confining stresses. The effective stress conditions during creep failure are also within the confidence interval of the failure criterion and do not deviate significantly from the observed laboratory short-term strengths. This observation deviates from the theory of brittle rock failure introduced by Bieniawski (1967), which suggests a considerably reduced strength resulting from creep deformation. Laboratory creep tests on a variety of rocks (i.e., sedimentary, metamorphic, and igneous rocks), showed creep failure at 70 % up to 95 % of the short-term strength supporting Bieniawski's theory (Paraskevopoulou, 2021; Y. Zhang et al., 2016; Q. Wang et al., 2020). These short-term strength

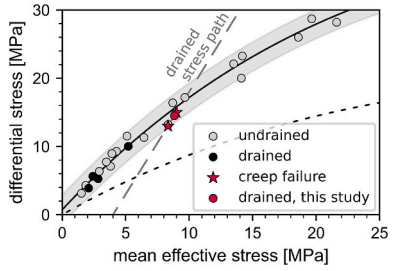

Fig. 12. *Failure criterion (solid line) of effective peak strength data from drained and undrained, consolidated triaxial shear tests (short-term: Winhausen et al., 2022; Wild and Amann, 2018a, 2018b; Minardi et al., 2021; this study) as well as the effective residual strength boundary (dashed line) of the shaly Opalinus Clay as a function of the differential stress (q) and the mean effective stress* $p' = (\sigma'_1 + \sigma'_2 + \sigma'_3)/3$ *(Winhausen et al., 2022). The stars indicate the stress conditions during creep failure (this study). The light grey shaded area is the confidence interval (95 %) of the dataset.*

values were obtained from laboratory tests performed within minutes. In studies on low permeability clay shales, however, extremely low compression rates in the order of 10^{-7} s^{-1} (undrained) and 10^{-8} s^{-1} (drained) are required to ensure a uniform pore pressure distribution within the specimens (e.g., Winhausen et al., 2022 and this study). As a result, drained shearing in low permeability clay shales can extend over several days (8.5 days for OPA10), raising the question of whether creep deformation may already influence the loading behavior of representative "short-term" experiments (Belmokhtar et al., 2018). Accordingly, the "short-term" strength observed in studies on OPA may already reflect reduced peak strength resulting from creep processes and, therefore, the creep failure (OPA1 and OPA2) stress conditions do not differ significantly from those of the short-term test (OPA10).

Since the creep behavior is a function of time, and longer time intervals allow continued recovery or continued accumulation of damage, the creep failure solely represents the rock strength observed within the experimental time scale of a few months. Yet, based on the previously discussed change in creep mechanisms (chapter 4.2), a threshold for potential creep failure can be proposed. Exceeding this stress threshold, damage progression and volumetric dilation are expected to dominate, eventually leading to creep failure when exposed to longer time scales (i.e., years). This threshold is 63 % (q = 10 MPa) of the fitted mean short-term peak strength ($q_{peak\text{-}fit} \approx 16$ MPa) and is therefore even lower than suggested by Bieniawski's theory. A verification of the exact stress conditions of this threshold requires more tests and longer experiments.

Creep failure of the specimens occurred under different stress conditions due to differences in the loading path and the test duration, but the onset of tertiary creep occurred at similar total cumulative axial strain (Fig. 4a). According to Kranz and Scholz (1977), the tertiary creep is initiated when a rock-specific critical strain is reached. In the present study, the observed critical axial strain is in the range of $0.71 \leq \varepsilon_{critical} \leq 0.75$ %, given as the sum of strain accumulation during loading and creep stages. This critical axial strain exceeds the axial strain at peak strength ($\varepsilon_{peak}[P] \approx 0.5$ %) obtained from drained and undrained short-term compression tests of other studies at similar effective confinement stresses on saturated OPA specimens (Winhausen et al., 2022; Minardi et al., 2021; Favero et al., 2018). However, the short-term reference test (OPA10) shows an axial strain accumulation of 0.72 % when reaching the peak strength (Fig. 5a), which is within the critical strain interval for the onset of tertiary creep. On the one hand, the sample variability (slightly weaker rock properties of OPA10) may contribute to an increased strain accumulation during short-term shearing. On the other hand, the development of failure at a similar strain accumulation can be attributed to exceeding the critical strain threshold, following the assumption that creep already occurs during the long-lasting shear phase.

In summary, the creep behavior of shaly OPA indicates two critical failure thresholds: The stress-related and the strain-related threshold. The stress threshold determines a change in the dominant creep mechanism from stress-insensitive and recovery-dominated processes to stress-sensitive and damage-dominated processes leading to potential failure over time. This potential failure occurs at a reduced strength compared to short-term loading and is referred to as the actual long-term strength of the clay shale. For saturated, shaly OPA this threshold is at a differential stress of approximately 10 MPa (~63 % of the average short-term peak strength) at an effective confining stress of 4 MPa. The strain threshold determines the onset of tertiary creep following the accumulation of a critical amount of strain over time. For saturated, shaly OPA this threshold is reached at a total cumulative axial strain of approximately 0.74 % at an effective confining stress of 4 MPa. Both thresholds are interdependent and equally relevant.

5. Conclusion

Long-term deformation is an important aspect of the performance assessment of nuclear waste repositories, which involves the characterization of the creep behavior under drained and fully saturated in-situ conditions. Therefore, a series of detailed multi-stage creep tests were carried out to investigate the creep behavior and the effective long-term strength of shaly Opalinus Clay considering different multi-stage loading paths. For the first time, the creep behavior of Opalinus Clay could be determined at precisely defined effective stress conditions. The experimental data provide significant input parameters for constitutive models of the shaly Opalinus Clay formation to perform numerical simulations of tunnel excavations in the context of nuclear waste storage.

Primary and secondary creep deformation occurred during all applied stress stages and no threshold for secondary creep was identified. This study highlights the importance of testing under fully saturated and consolidated conditions since, five to ten times faster secondary creep rates were observed compared to previous studies conducted on partially saturated shaly OPA (Naumann et al., 2007; Gräsle and Plischke, 2010). Thus, the creep potential of shaly OPA was underestimated by previous studies.

The secondary creep rates increased exponentially with increasing differential stress. This exponential development can be categorized into a stress-insensitive and a stress-sensitive creep behavior, which is associated with a change in the dominant underlying creep mechanism. At low differential stress ($q \leq 10$ MPa, $\sigma_c' = 4\ MPa$), the processes are stress-insensitive and dominated by strengthening recovery-processes, potentially governed by diffusion creep. At high differential stress ($q \geq 10$ MPa, $\sigma_c' = 4\ MPa$), the processes are stress-sensitive and dominated by weakening damage-processes, accompanied by progressive microcracking.

A stress-dependent and a strain-dependent threshold for potential creep failure are defined. The stress threshold ($q_{\text{long-term\_strength}} = 10$ MPa for $\sigma_c' = 4\ MPa$) predicts the long-term strength, which is significantly lower than the observed short-term strength of the shaly Opalinus Clay. By exceeding this threshold, the creep mechanisms lead to increased damage accumulation. The strain threshold ($\varepsilon_{critical} = 0.74$ % for $\sigma_c' = 4\ MPa$) predicts the critical strain accumulation which leads to the onset of tertiary creep over time.

This study demonstrates that creep deformation is significant and relevant under in-situ conditions (drained and fully saturated) and must be anticipated around excavations in clay shales such as the Opalinus Clay. The understanding of creep mechanisms is crucial to predict distinct time-dependent convergence at the excavation scale to isolate deformation stemming from consolidation or creep. In particular, the potential for delayed failure at reduced strength holds a risk to safety and stability over time and must be considered in construction designs and lining properties. An underestimation of creep deformation and the overestimation of the long-term strength leads to increased geo-engineering risks regarding the long-term integrity of nuclear waste repositories.

Statement

During the preparation of this work the authors used *DeepL Write* in order to improve readability and language. After using *DeepL Write*, the authors reviewed and edited the content as needed and take full responsibility for the content of the published article.

CRediT authorship contribution statement

Lina Gotzen: Conceptualization, Writing – review & editing, Writing – original draft, Visualization, Methodology, Investigation, Formal analysis, Data curation. **Lisa Winhausen:** Conceptualization, Writing – review & editing, Supervision, Methodology. **Mohammadreza Jalali:** Conceptualization, Writing – review & editing. **Kavan Khaledi:** Conceptualization, Writing – review & editing. **Florian Amann:** Conceptualization, Writing – review & editing, Supervision, Project

administration, Funding acquisition.

Declaration of competing interest

The contact author has declared that neither they nor their co-authors have any competing interests.

Acknowledgements

We would like to thank the Swiss Federal Nuclear Safety Inspectorate (ENSI) for financial support for a project entitled “Development and Validation of a Constitutive Model for Opalinus Clay”. We thank Timo Seemann for the performance and analysis of XRD measurements of the specimens.

Appendix A. Supplementary data

Supplementary data to this article can be found online at https://doi.org/10.1016/j.enggeo.2025.107961.

Data availability

The database containing the laboratory testing results can be accessed via DOI: 10.18154/RWTH-2025-01319.

References

Amann, F., Wild, K.M., Loew, S., Yong, S., Thoeny, R., Frank, E., 2017. Geomechanical behaviour of Opalinus Clay at multiple scales: results from Mont Terri Rock laboratory (Switzerland). Swiss J. Geosci. 110 (1), 151–171. https://doi.org/10.1007/s00015-016-0245-0.

Aristorenas, G.V., 1992. Time-Dependent Behavior of Tunnels Excavated in Shale. Thesis. Massachusetts Institute of Technology. https://dspace.mit.edu/handle/1721.1/13197.

Armand, G., Noiret, A., Zghondi, J., Seyedi, D.M., 2013. Short- and long-term behaviors of drifts in the Callovo-Oxfordian claystone at the Meuse/Haute-Marne underground research laboratory. J. Rock Mech. Geotech. Eng. 5 (3), 221–230. https://doi.org/10.1016/j.jrmge.2013.05.005.

Atkinson, B.K., 1984. Subcritical crack growth in geological materials. J. Geophys. Res. Solid Earth 89 (B6), 4077–4114. https://doi.org/10.1029/JB089iB06p04077.

Barla, G., 2001. Tunnelling under squeezing rock conditions. In: Tunnelling Mechanics-Advances in Geotechnical Engineering and Tunnelling- In: Eurosummer-School in Tunnel Mechanics. Innsbruck, Logos Verlag, Berlin, pp. 169–268.

Belmokhtar, M., Delage, P., Ghabezloo, S., Conil, N., 2018. Drained triaxial tests in low-permeability shales: application to the Callovo-Oxfordian claystone. Rock Mech. Rock. Eng. 51 (7), 1979–1993. https://doi.org/10.1007/s00603-018-1442-0.

Bieniawski, Z.T., 1967. Mechanism of brittle fracture of rock - part3- fracture in tension and under long-term loading. Int. J. Rock Mech. Min. Sci. 4, 423–430.

Bishop, A.W., Henkel, D.J., 1962. The Measurement of Soil Properties in the Triaxial Test, 2. ed., Reprinted. Arnold, London.

Bossart, P., Bernier, F., Birkholzer, J., Bruggeman, C., Connolly, P., Dewonck, S., Fukaya, M., et al., 2017. Mont Terri Rock laboratory, 20 years of research: introduction, site characteristics and overview of experiments. Swiss J. Geosci. 110 (1), 3–22. https://doi.org/10.1007/s00015-016-0236-1.

Brantut, N., Baud, P., Heap, M.J., Meredith, P.G., 2012. Micromechanics of brittle creep in rocks. J. Geophys. Res. Solid Earth 117 (B8), 2012JB009299. https://doi.org/10.1029/2012JB009299.

Bui, H.N., Hull, T., Small, J.C., 2001. Secondary Compression of Clays. Department of Civil Engineering.

Casagrande, A., Fadum, R.E., 1940. “Notes on Soil Testing for Engineering Purposes,” Soil Mechanics Series, No.8.

Cristescu, N., Hunsche, U., 1998. Time effects in rock mechanics. In: Wiley Series in Materials, Modelling and Computation. Wiley, Chichester; New York.

Dusseault, M.B., Fordham, C.J., 1993. Time-dependent behavior of rocks. In: Rock Testing and Site Characterization. Elsevier, pp. 119–149. https://doi.org/10.1016/B978-0-08-042066-0.50013-6.

Einstein, H.H., 2000. Tunnels in Opalinus Clayshale — a review of case histories and new developments. Tunn. Undergr. Space Technol. 15 (1), 13–29. https://doi.org/10.1016/S0886-7798(00)00025-0.

Fabre, G., Pellet, F., 2006. Creep and time-dependent damage in argillaceous rocks. Int. J. Rock Mech. Min. Sci. 43 (6), 950–960. https://doi.org/10.1016/j.ijrmms.2006.02.004.

Favero, V., Ferarri, A., Laloui, L., 2018. Anisotropic behaviour of Opalinus Clay through consolidationed and drained triaxial testing in saturated consitions. Rock Mech. Rock. Eng. 51, 1305–1319. https://doi.org/10.1007/s00603-017-1398-5.

Ferrari, A., Favero, V., Laloui, L., 2016. One-dimensional compression and consolidation of shales. Int. J. Rock Mech. Min. Sci. 88 (October), 286–300. https://doi.org/10.1016/j.ijrmms.2016.07.030.

Gasc-Barbier, M., Chanchole, S., Bérest, P., 2004. Creep behavior of bure clayey rock. Appl. Clay Sci. 26 (1–4), 449–458. https://doi.org/10.1016/j.clay.2003.12.030.

Geng, Z., Bonnelye, A., Chen, M., Jin, Y., Dick, P., David, C., Fang, X., Schubnel, A., 2018. Time and temperature dependent creep in Tournemire Shale. J. Geophys. Res. Solid Earth 123 (11), 9658–9675. https://doi.org/10.1029/2018JB016169.

Geng, Z., Bonnelye, A., David, C., Dick, P., Wang, Y., Schubnel, A., 2021. Pressure solution compaction during creep deformation of Tournemire Shale: implications for temporal sealing in shales. J. Geophys. Res. Solid Earth 126 (3). https://doi.org/10.1029/2020JB021370.

Golan, O., Arbel, A., Eliezer, D., Moreno, D., 1996. The applicability of Norton’s creep power law and its modified version to a single-crystal superalloy type CMSX-2. Mater. Sci. Eng. A 216 (1–2), 125–130. https://doi.org/10.1016/0921-5093(96)10400-7.

Gräsle, W., Plischke, I., 2010. Mont Terri Project - Laboratory Testing (LT) Experiment: Mechanical Behavior of Opalinus Clay. Final Report from Phases 6–14.” TR2009–07. BGR, Germany.

Head, K.H., 1998. Manual of Soil Laboratory Testing. Vol3 - Effective Stress Tests, 2. ed. Pentech Pr, London.

Head, K.H., Epps, R.J., 2011. Manual of Soil Laboratory Testing: Vol2 - Permeability. Shear Strength and Compressibility Tests, 3rd ed. Whittels Publishing, Scotland, UK.

Herrmann, J., Rybacki, E., Sone, H., Dresen, G., 2020. Deformation experiments on Bowland and Posidonia Shale—part II: creep behavior at in situ Pc–T conditions. Rock Mech. Rock. Eng. 53 (2), 755–779. https://doi.org/10.1007/s00603-019-01941-2.

Kranz, R.L., 1979. Crack growth and development during creep of Barre granite. Int. J. Rock Mech. Min. Sci. Geomech. Abstr. 16 (1), 23–35. https://doi.org/10.1016/0148-9062(79)90772-1.

Kranz, R.L., Scholz, C.H., 1977. Critical dilatant volume of rocks at the onset of tertiary creep. J. Geophys. Res. 82 (30), 4893–4898. https://doi.org/10.1029/JB082i030p04893.

Lauper, B., Zimmerli, G.N., Jaeggi, D., Deplazes, G., Wohlwend, S., Rempfer, J., Foubert, A., 2021. Quantification of lithological heterogeneity within Opalinus Clay: toward a uniform subfacies classification scheme using a novel automated core image recognition tool. Front. Earth Sci. 9 (May), 645596. https://doi.org/10.3389/feart.2021.645596.

Leone, T., Nordas, A.N., Anagnostou, G., 2024. Creep versus consolidation in tunnelling through squeezing ground—part a: basic time effects. Rock Mech. Rock. Eng. 57 (8), 5519–5536. https://doi.org/10.1007/s00603-023-03720-6.

Li, Y., Q., Hu, N., Wu, Wang, H., Sun, X., G., Hu, Sun, Z., Jiang, Y., 2023. Acoustic characterization for creep behaviors of marine sandy hydrate-bearing sediment. Sci. Rep. 13 (1), 22199. https://doi.org/10.1038/s41598-023-49523-1.

Mäder, U., 2011. “Recipe and Preparation of Simplified Artificial Pore Wter for ‘Opalinus Clay’ and ‘Brown Dogger’ Based on the Nagra Reference Pore Water Composition, Containing Na-K-Ca-Mg-Cl-SO4-HCO3, and Adjusted at Atmospheric P-CO2.” Nagra.

Mánica, M., Gens, A., Vaunat, J., Ruiz, D., 2017. A time-dependent anisotropic model for argillaceous rocks. Application to an underground excavation in Callovo-Oxfordian claystone. Comput. Geotech. 85, 341–350.

Marschall, P., Croisé, J., Schlickenrieder, L., Boisson, J.Y., Vogel, P., Yamamoto, S., 2003. “Mont Terri Project - Synthesis of Hydrogeological Investigations at the Mont Terri Site (Phases 1 to 5).” TR2001–02.

Masset, O., 2006. “Mont Terri Project - Rock Laboratory Pore Pressure Long Term Evolution.” 21-TN2006_43.

Mazurek, M., Hurford, A.J., Leu, W., 2006. Unravelling the multi-stage burial history of the Swiss Molasse Basin: integration of apatite fission track, vitrinite reflectance and biomarker isomerisation analysis. Basin Res. 18 (1), 27–50. https://doi.org/10.1111/j.1365-2117.2006.00286.x.

Minardi, A., Giger, S.B., Ewy, R.T., Stankovic, R., Stenebråten, J., Soldal, M., Rosone, M., Ferrari, A., Laloui, L., 2021. Benchmark study of undrained triaxial testing of Opalinus Clay Shale: results and implications for robust testing. Geomech. Energy Environ. 25 (March), 100210. https://doi.org/10.1016/j.gete.2020.100210.

Moore, D.M., Reynolds, R.C., 1989. X-Ray Diffraction and the Identification and Analysis of Clay Minerals. Oxford University Press, Oxford [England]; New York.

Naumann, M., Hunsche, U., Schulze, O., 2007. Experimental investigations on anisotropy in dilatancy, failure and creep of Opalinus Clay. Phys. Chem. Earth Parts A/B/C 32 (8–14), 889–895. https://doi.org/10.1016/j.pce.2005.04.006.

Nordas, A.N., Leone, T., Anagnostou, G., 2024. Creep versus consolidation in tunnelling through squeezing ground—part B: transferability of experience. Rock Mech. Rock. Eng. 57 (8), 5537–5555. https://doi.org/10.1007/s00603-024-03968-6.

Norton, F.H., 1929. The Creep of Steel at High Temperatures. McGraw-Hill Book Company, New York.

Paraskevopoulou, C., 2021. Time-dependent behavior of rock materials. In: Lwisa, E., Arman, H. (Eds.), Engineering Geology. IntechOpen. https://doi.org/10.5772/intechopen.96997.

Pearson, F.J., Arcos, D., Bath, A., Boisson, J.Y., Fernandez, A.M., Gäbler, H.D., Gaucher, E., 2003. “Geochemistry of Water in the Opalinus Clay Formation at the Mont Terri Laboratory.” Technical Report TR 2003–03. Mont Terri Project. https://www.mont-terri.ch/en/documentation/technical-reports.detail.document.html/mont-terri-internet/en/documents/technical-reports/TR2003-03.pdf.html.

Pusch, R., Hökmark, H., 1992. Mechanisms and Consequences of a Creep in the Nearfield Rock of a KBS-3 Repository. Technical Report TR 93-10.. SKB - Swedish Nuclear Fuel and Waste Management Co., Stockholm https://www.skb.com/publication/9261.

Rybacki, E., Dresen, G., 2000. Dislocation and diffusion creep of synthetic anorthite aggregates. J. Geophys. Res. 105 (B11).

Rybacki, E., Herrmann, J., Wirth, R., Dresen, G., 2017. Creep of Posidonia Shale at elevated pressure and temperature. Rock Mech. Rock. Eng. 50 (12), 3121–3140. https://doi.org/10.1007/s00603-017-1295-y.

Skempton, A.W., 1954. The pore-pressure coefficients A and B. Géotechnique 4 (4), 143–147. https://doi.org/10.1680/geot.1954.4.4.143.
Sone, H., Zoback, M.D., 2014. Time-dependent deformation of shale gas reservoir rocks and its long-term effect on the in situ state of stress. Int. J. Rock Mech. Min. Sci. 69 (July), 120–132. https://doi.org/10.1016/j.ijrmms.2014.04.002.
Spiers, C.J., Schutjens, P.M.T.M., Brzesowsky, R.H., Peach, C.J., Liezenberg, J.L., Zwart, H.J., 1990. Experimental determination of constitutive parameters governing creep of rocksalt by pressure solution. Geol. Soc. Lond. Spec. Publ. 54 (1), 215–227. https://doi.org/10.1144/GSL.SP.1990.054.01.21.
Środoń, J., 1980. Precise identification of illite/smectite interstratifications by x-ray powder diffraction. Clay Clay Miner. 28 (6), 401–411. https://doi.org/10.1346/CCMN.1980.0280601.
Taylor, D.W., Merchant, W., 1940. A theory of clay consolidation accounting for secondary compression. J. Math. Phys. 19 (1–4), 167–185. https://doi.org/10.1002/sapm1940191167.
Terzaghi, K., 1943. Theoretical Soil Mechanics. John Wiley & Sons, Inc., Hoboken, NJ, USA https://doi.org/10.1002/9780470172766.
Wang, Q., Hu, X., Xu, C., Zhou, C., He, C., Ying, C., 2020. Time-dependent behavior of saturated silty mudstone under different confining pressures. Bull. Eng. Geol. Environ. 79 (5), 2621–2634. https://doi.org/10.1007/s10064-020-01728-8.
Wang, H., Cui, Y.J., Vu, M.N., Zhang, F., Talandier, J., 2023. On the hydro-mechanical behaviour of unsaturated damaged Callovo-Oxfordian claystone. Eng. Geol. 319 (June), 107107. https://doi.org/10.1016/j.enggeo.2023.107107.
Wild, K.M., Amann, F., 2018a. Experimental study of the hydro-mechanical response of Opalinus Clay – part 1: pore pressure response and effective geomechanical properties under consideration of confinement and anisotropy. Eng. Geol. 237 (April), 32–41. https://doi.org/10.1016/j.enggeo.2018.02.012.
Wild, K.M., Amann, F., 2018b. Experimental study of the hydro-mechanical response of Opalinus Clay – part 2: influence of the stress path on the pore pressure response. Eng. Geol. 237 (April), 92–101. https://doi.org/10.1016/j.enggeo.2018.02.011.
Wild, K.M., Wymann, L.P., Zimmer, S., Thoeny, R., Amann, F., 2015. Water retention characteristics and state-dependent mechanical and petro-physical properties of a clay shale. Rock Mech. Rock. Eng. 48 (2), 427–439. https://doi.org/10.1007/s00603-014-0565-1.
Wild, K.M., Barla, M., Turinetti, G., Amann, F., 2017. A multi-stage triaxial testing procedure for low permeable geomaterials applied to Opalinus Clay. J. Rock Mech. Geotech. Eng. 9 (3), 519–530. https://doi.org/10.1016/j.jrmge.2017.04.003.
Winhausen, L., Amann-Hildenbrand, A., Fink, R., Jalali, M., Khaledi, K., Hamdi, P., Urai, J.L., Schmatz, J., Amann, F., 2021. A comparative study on methods for determining the hydraulic properties of a clay shale. Geophys. J. Int. 224 (3), 1523–1539. https://doi.org/10.1093/gji/ggaa532.
Winhausen, L., Khaledi, K., Jalali, M., Urai, J.L., Amann, F., 2022. Failure mode transition in Opalinus Clay: a hydro-mechanical and microstructural perspective. Solid Earth 13 (5), 901–915. https://doi.org/10.5194/se-13-901-2022.
Yu, H.D., Chen, W.Z., Gong, Z., Tan, X.J., Ma, Y.S., Li, X.L., Sillen, X., 2015. Creep behavior of boom clay. Int. J. Rock Mech. Min. Sci. 76 (June), 256–264. https://doi.org/10.1016/j.ijrmms.2015.03.009.
Yu, H.D., Lu, C., Chen, W.Z., Tian, H.M., 2021. An insight into the creep mechanisms of a clayey soil through long-term consolidation tests. Bull. Eng. Geol. Environ. 80 (12), 9127–9139. https://doi.org/10.1007/s10064-021-02472-3.
Yu, H.D., Chen, W.Z., Ma, Y.S., Tan, X.J., Yang, J.P., 2023. Experimental and theoretical study on the creep behavior of a clayey rock. Rock Mech. Rock. Eng. 56 (2), 1387–1398. https://doi.org/10.1007/s00603-022-03146-6.
Zhang, C.L. (Ed.), 2013. Thermo-Hydro-Mechanical Processes in the Nearfield around a HLW Repository in Argillaceous Formations. Vol. 1: Laboratory Investigations. Vol. 1. GRS 312. GRS, Köln.
Zhang, C.L., Laurich, B., 2020. Mechanical behavior of sandy facies of Opalinus Clay under different load conditions. J. Rock Mech. Geotech. Eng. 12 (2), 223–241. https://doi.org/10.1016/j.jrmge.2019.09.005.
Zhang, Y., Shao, J., Xu, W., Jia, Y., 2016. Time-dependent behavior of cataclastic rocks in a multi-loading triaxial creep test. Rock Mech. Rock. Eng. 49 (9), 3793–3803. https://doi.org/10.1007/s00603-016-0948-6.